Joule

CellPress

Article

Efficient Perovskite Solar Cell Modules with High Stability Enabled by Iodide Diffusion Barriers

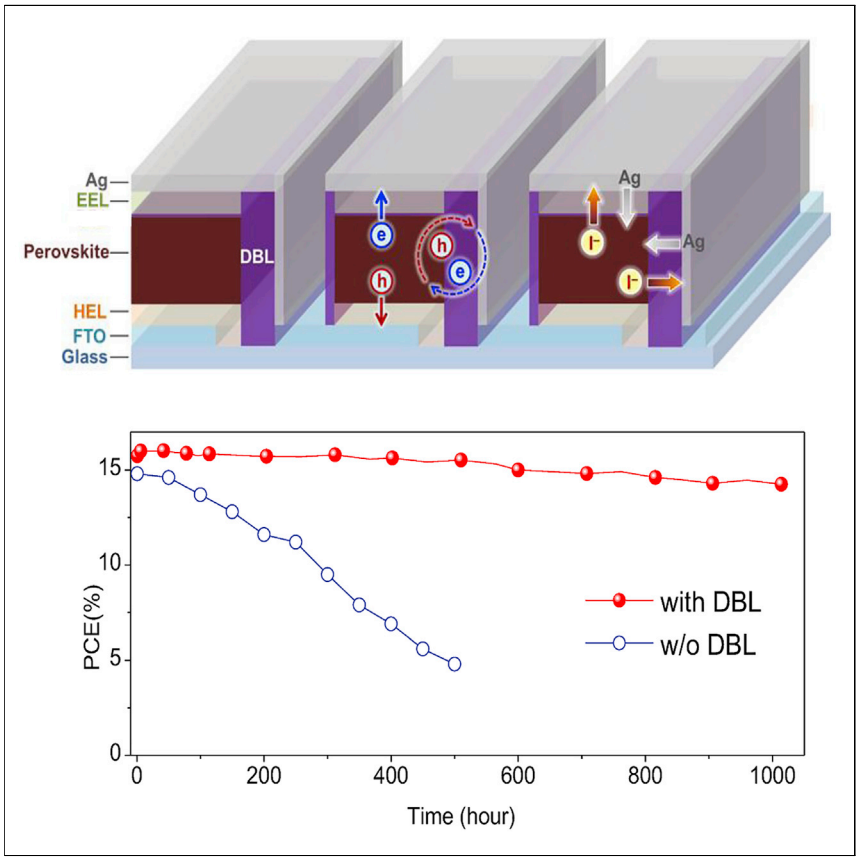

Operational stability is crucial for the success in large-scale application of metal halide perovskites devices. The diffusion of volatile iodide component of perovskites can induce irreversible device degradation. Here, low-dimensional diffusion barriers were introduced to increase the operational stability of high-efficiency large-area PSC modules. A negligible decay was observed after 1,000 h under severe test condition for a 15% high-efficiency solar module.

Enbing Bi, Wentao Tang, Han Chen, ..., Xudong Yang, Michael Grätzel, Liyuan Han

yang.xudong@sjtu.edu.cn (X.Y.)
han.liyuan@sjtu.edu.cn (L.H.)

HIGHLIGHTS

Effective low-dimensional diffusion barriers were realized at low-temperature processing

Unwanted ions diffusion reduced by 10^3–10^7 times in magnitude

Thermally stable perovskite solar modules at 85°C for over 1,000 h were achieved

Bi et al., Joule 3, 2748–2760
November 20, 2019
https://doi.org/10.1016/j.joule.2019.07.030

Joule

CellPress

Article

Efficient Perovskite Solar Cell Modules with High Stability Enabled by Iodide Diffusion Barriers

Enbing Bi,[1,2,3,9] Wentao Tang,[1,9] Han Chen,[1,9] Yanbo Wang,[1] Julien Barbaud,[1] Tianhao Wu,[1] Weiyu Kong,[1] Peng Tu,[4] Hong Zhu,[4] Xiaoqin Zeng,[5] Jinjin He,[1] Shin-ichi Kan,[6] Xudong Yang,[1,2,*] Michael Grätzel,[7] and Liyuan Han[1,2,8,10,*]

SUMMARY

Operational stability of efficient opto-electronic conversion is crucial for the success in large-scale application of perovskites devices. Owing to the intrinsically weak structure of perovskites, iodide represents the most volatile constituents, and its diffusion can induce irreversible degradation that continues to present a great challenge to realize stable perovskite devices. Here, we introduce a low-temperature processing strategy to increase the operational stability of high-efficiency perovskite solar modules by engineering low-dimensional diffusion barriers, reducing the unwanted interfacial diffusion of ions by 10^3–10^7 times in magnitude. We finally achieved stable and efficient perovskite solar modules with an area of 36 cm^2 retaining over 95% of their initial efficiency of over 15% after 1,000 h of heating at 85°C, and 91% after light soaking in AM 1.5 G solar light for 1,000 h, respectively. Our findings provide an effective strategy to realize operationally stable and efficient perovskite solar cell modules.

INTRODUCTION

Metal halide perovskite solar cells (PSCs) have attracted great attention owing to their excellent photovoltaic properties.[1–5] Various strategies have been successfully implemented to enhance the device performance,[6–15] remarkably with compositional,[16–18] interfacial,[19–21] dimensional[22,23] and architectural engineering,[24,25] etc. The certified power conversion efficiency (PCE) has advanced rapidly to 24.2%, exceeding that of top-level polycrystalline silicon solar cells. However, high-efficiency PSCs are generally unstable, which continues to present a major challenge for future large-scale application.[26,27] The major instability issue is attributed to the intrinsically weak bonding of halide perovskite materials where iodide represents the most volatile constituents with the diffusion coefficient as high as $\sim 10^{-12}$ cm^2 s^{-1},[28–30] leading to a significant decomposition of perovskite structure and a fast decline in the device performance.[31,32] These diffusion-induced degradation processes can be further accelerated in working devices by light, heat, electric field, moisture, air, or lattice strain[29–33] as well as for other perovskite-based optoelectronic devices like light-emitting diodes, photodetectors, laser diodes, etc. Therefore, it is highly desired to control the diffusion process in high-efficiency perovskite devices for the realization of long-term operational stability.

The stability of high-efficiency perovskite solar cell modules (PSC modules) is much poorer than that of small-area PSCs,[34] indicating a more complex degradation

Context & Scale

Perovskite solar cell has advanced rapidly with power conversion efficiency exceeding 24%, which makes it a promising candidate for a high-performance, low-cost photovoltaic technology. However, the large-scale perovskite solar module suffered from more serious durability problems than that of the small-area devices due to a more complex degradation mechanism introduced by iodide diffusion. It is highly desired to control the iodide diffusion process in high-efficiency perovskite devices for the realization of long-term stability. Here, we report a low-temperature solution-process-based strategy to realize stable and efficient perovskite solar modules with low-dimensional diffusion barriers. Using this strategy, the extra diffusion-induced degradation of perovskite solar modules was largely suppressed. Our findings are crucial for the design and realization of highly stable and efficient perovskite solar modules and other large-area perovskite-based optoelectronic devices.

mechanism taking effect. Generally, high-efficiency PSC modules contain a sub-cell array with series interconnections where the perovskite film is scribed and partially exposed to a metal electrode or air. These unwanted contacts provide extra channels for iodide diffusion in PSC modules, even though the ingression of moist air can be excluded by careful encapsulation. Therefore, two major iodide diffusion channels within the PSC modules need to be suppressed (Figure 1A). The first is the vertical diffusion that is commonly observed in small-area PSCs or other halide perovskite optoelectronic devices where iodide diffuses perpendicularly to the substrate surface in the active area.[31,35] The second is the lateral diffusion that occurs parallel to the substrate at the interconnects between the sub-cells or other pixel array devices,[36,37] which has produced a serious stability predicament on the module scale. However, rare research has been reported simultaneously overcoming these diffusion-induced degradation processes within the high-efficiency PSC module. In addition, any procedure envisaged to block the unwanted vertical and lateral diffusion process should avoid high temperatures as the perovskite film decomposes under heat.[38,39]

Here, we report a low-temperature solution-process-based strategy to realize stable and efficient PSC modules with low-dimensional diffusion barriers (DBLs). We block the diffusion channels by introducing zero-dimensional (0D), one-dimensional (1D), and two-dimensional (2D) DBLs that consist of chemically and thermally stable metal oxide nanoparticles, inert silicon-based organic polymers, and two-dimensional nano-structured inorganic materials, respectively. Using this strategy, we reduce the leakage rate of iodide by $10^3 \sim 10^7$ times. Moreover, owing to the defect passivation effect of the DBL, the non-radiation recombination of photogenerated carriers at the perovskite surface was reduced. These findings enabled us to obtain stable PSC modules with an efficiency of 15.6% at an aperture area of 36 cm^2, which maintained 95% of their initial PCE after 1,000 h of heating aging at 85°C and 91% after 1,000 h light-soaking at maximum power point tracking under AM 1.5 G solar light. To the best of our knowledge, this is the first time that a PSC module simultaneously obtained an efficiency of over 15% and heating as well as operational stability over 1,000 h. This work provides a promising way to realize long-term stability for high-efficiency PSC modules or other large-area perovskite-based optoelectronic devices.

RESULTS AND DISCUSSION

A schematic presentation of our DBLs is given in Figure 1. The 0D-DBL consists of Al_2O_3 nanoparticles (Figure 1B) that exhibit high thermal and chemical stability. The candidate for 1D-DBL is polydimethylsiloxane (PDMS, Figure 1C), which is chemically stable and can easily form a smooth layer. We choose tri-s-triazine-based graphitic carbon nitride (g-C_3N_4, Figure 1D) nanosheets to form 2D-DBL. All the functionalized DBLs were dissolved or dispersed in solutions for low-temperature processing, which was cured by cationic photopolymerization to enhance the mechanical properties and strength of adhesion. The $MAPbI_3$ film was used for the material study because of its poor stability compared to the mixed FA-based perovskite to demonstrate which kind of material will have a higher effect on hindering ion diffusion.

We quantified the extent of reduction of the diffusion process, involving the present PSC configuration with mainly Ag particles and iodide anions, by detecting the distribution of these elements within thermally aged Ag/DBL/perovskite film. Figure 1E shows the depth profile of iodide and Ag concentrations in the Ag /0D-DBL/perovskite film, which

[1]State Key Laboratory of Metal Matrix Composites, School of Materials, Science and Engineering, Shanghai Jiao Tong University, 800 Dong Chuan RD. Minhang District, Shanghai 200240, China

[2]Joint Research Center for Clean Energy Materials, School of Materials Science and Engineering, Shanghai Jiao Tong University, 800 Dong Chuan RD. Minhang District, Shanghai 200240, China

[3]Shanghai Liyuan New Energy Technology Co.,Ltd, No.1599 Fengpu Avenue, Fengxian District, Shanghai 201400, China

[4]University of Michigan, Shanghai Jiao Tong University Joint Institute, Shanghai Jiao Tong University, 800 Dongchuan RD, Minhang District, Shanghai 200240, China

[5]Shanghai Engineering Research Center of Magnesium Materials and Applications, School of Materials, Science and Engineering, Shanghai Jiao Tong University, 800 Dong Chuan RD. Minhang District, Shanghai 200240, China

[6]Department of Electronic Science and Engineering, Kyoto University, Katsura, Nishikyo-ku, Kyoto 615-8520, Japan

[7]Laboratory of Photonics and Interfaces, Institute of Chemical and Engineering Science, Swiss Federal Institute of Technology, Station 6, CH–1015 Lausanne, Switzerland

[8]Photovoltaic Materials Group, Center for Green Research on Energy and Environmental Materials, National Institute for Materials Science, Tsukuba, Ibaraki 305-0047, Japan

[9]These authors contributed equally

[10]Lead Contact

*Correspondence: yang.xudong@sjtu.edu.cn (X.Y.), han.liyuan@sjtu.edu.cn (L.H.)

https://doi.org/10.1016/j.joule.2019.07.030

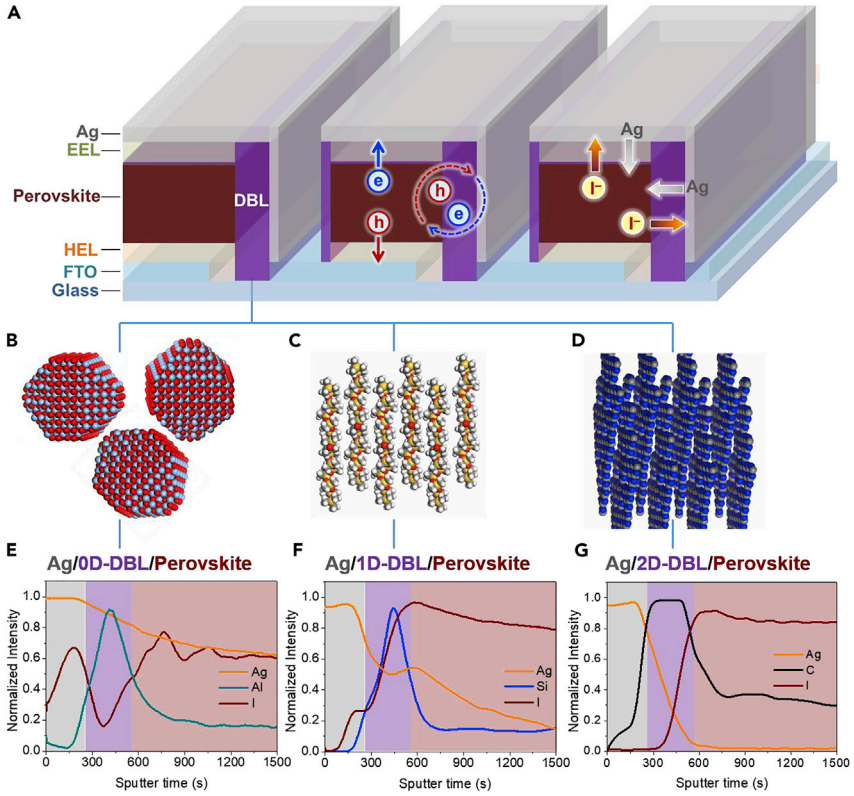

Figure 1. Schematic Illustration of Diffusion Barriers within Perovskite Solar Cell Modules (Psc Modules)

(A) Illustration of the diffusion process and interfacial charge transfer (solid lines) and recombination (dotted circle) in PSC module (EEL is the electron extraction layer and HEL is the hole extraction layer).

(B) Al_2O_3 nanoparticles for 0D-DBL.

(C) Polydimethylsiloxane (PDMS) for 1D-DBL.

(D–G) Graphitic carbon nitride (g-C_3N_4) for 2D-DBL (D). The depth profile of diffused iodide and Ag in (E) Ag /0D-DBL/perovskite film with aluminum signal, (F) Ag /1D-DBL/ perovskite film with silicon signal, and (G) Ag/2D-DBL/ perovskite film with carbon signal, respectively.

was determined by time of flight secondary ion mass spectrometry (ToF-SIMS). A large amount of iodide and Ag co-exist through the film, indicating that the diffusion process was still quite serious even if it was attenuated by 0D-DBL. For the Ag/1D-DBL/perovskite film, the penetration of iodide into the Ag film and that of Ag into the perovskite was largely reduced (Figure 1F). Finally, for 2D-DBL, the extent of interfacial iodide and Ag diffusion was negligible (Figure 1G).

The scanning electron microscopy with energy dispersive X-ray (SEM-EDX) measurements were conducted to probe the iodide distribution in lateral structured perovskite/DBL preheated at a temperature of 100°C in the dark and dry conditions for 900 h. It indicated that the iodide laterally diffused across the whole 0D-DBL film and two-thirds of the 1D-DBL film (Figures 2A and 2B), while it was almost hindered by 2D-DBL (Figure 2C). In the line intensity of EDX in Figures 2D–2F, we can find that the distribution of iodide element across from perovskite to 0D-DBL and 1 D-DBL film shows a graded distribution in the lateral structured perovskite/DBL film. These results demonstrate that 2D-DBL has an outstanding capability to protect the Ag electrode from iodide erosion via suppressing the interlayer diffusion process.

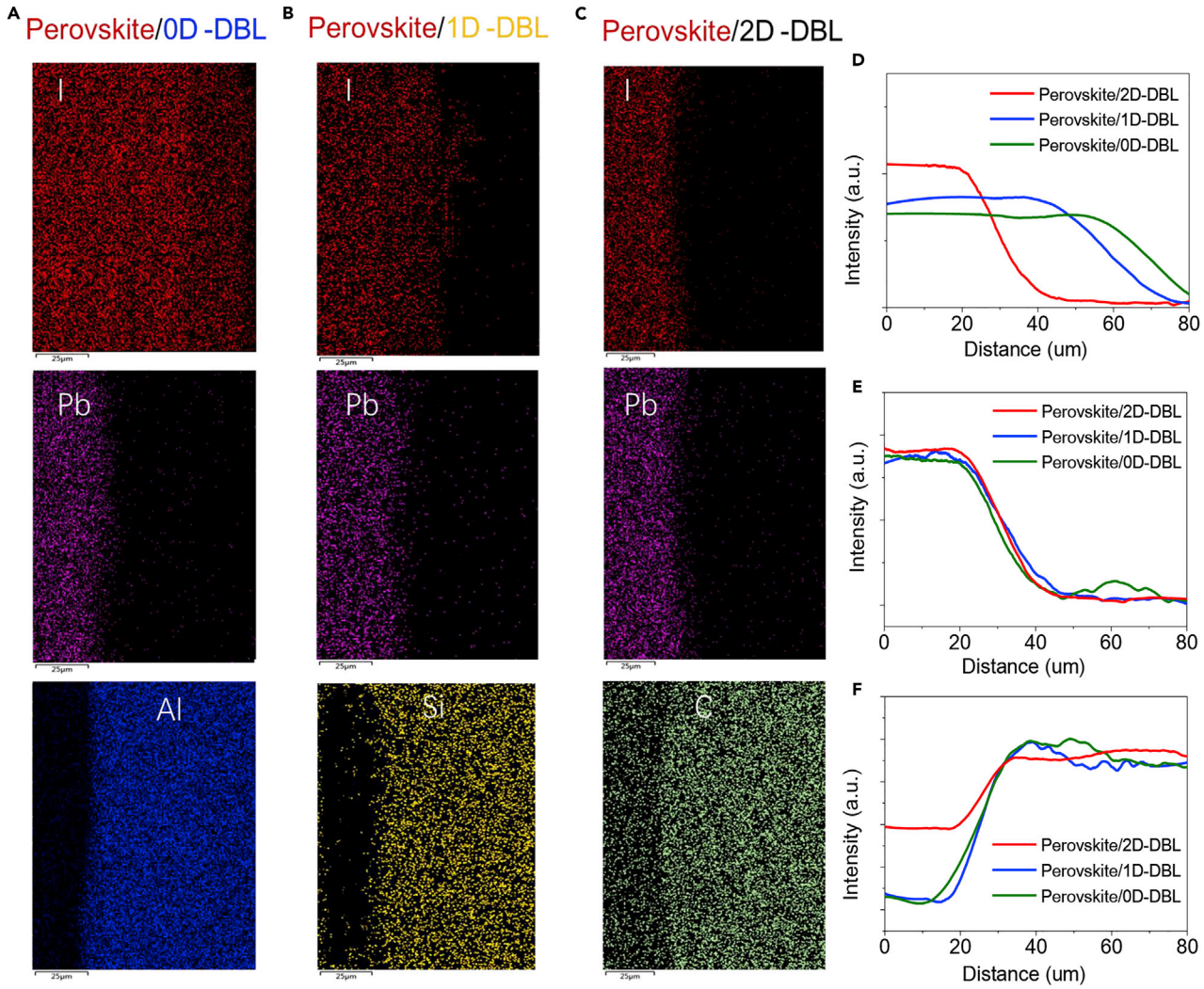

Figure 2. Monitoring Iodide Distribution in Lateral Structured Perovskite/DBL

(A–C) SEM-EDX analysis of iodide lateral diffused across 0D-DBL (A), 1D-DBL (B), and 2D-DBL (C). The lateral structured perovskite/DBLs film were preheated at temperature of 100°C in the dark and dry conditions for 900 h.

(D–F) The different elements intensity distribution of EDX line scanning for lateral structured perovskite/DBL based on 0D-DBL (D), 1D-DBL (E), and 2D-DBL (F). The scanning positions were across in the SEM-EDX image. Scale bar, 25 μm.

We measured the absorbance spectra of perovskite films to estimate the decomposition induced by the loss of iodide. HI and CH_3NH_2 being the predominant volatile decomposition products, their loss induces the conversion of $CH_3NH_3PbI_3$ to PbI_2 reducing the light absorbance above 600 nm.[37,40] As shown in Figure S1, the color of the perovskite films without DBLs turned from dark brown to yellow and the characteristic light absorbance at a wavelength of over 600 nm was almost lost after the aging test (Figure S2). Under the protection by DBLs, the change in color became slower and there was only negligible loss of light absorbance for films with 1D and 2D-DBL. The film of perovskite/2D-DBL also exhibited negligible change under ultraviolet radiation for 200 h (Figure S3), which indicates no obvious photocatalysis at the junction between perovskite and 2D-DBL. As given in Figure S4, the light absorbance at wavelength of 600 nm is directly proportional to the amount of perovskite when the ratio of CH_3NH_3I:PbI_2 is in the range of 0.8 to 1.0. A similar trend was also found at a wavelength of 700 and 750 nm. These results indicate that we can

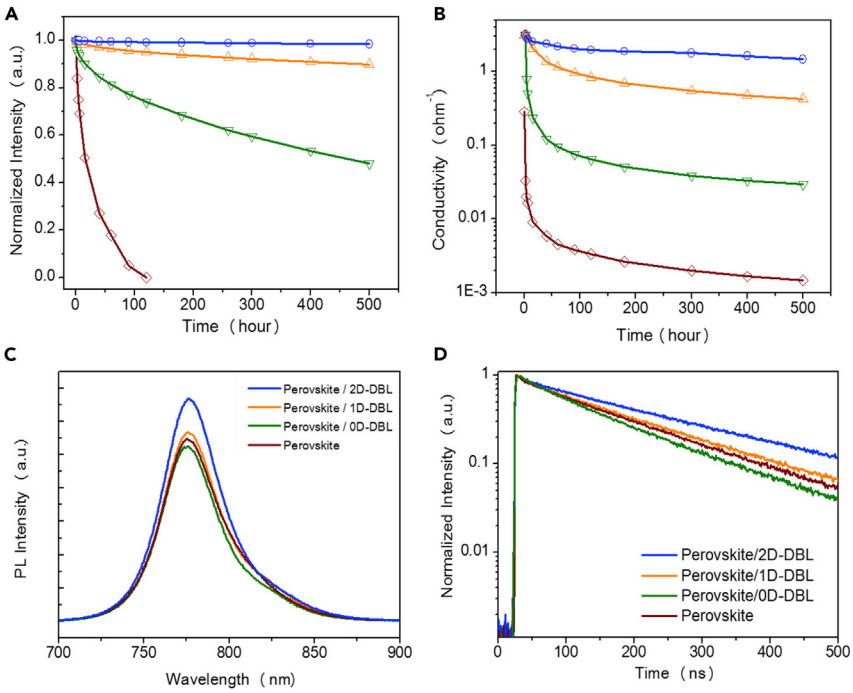

Figure 3. Effect of Diffusion Barriers on the Light Absorbance, Electronic Conductivity, and Photoluminescence

(A) The normalized light absorbance of perovskite films with 0D-DBL (down-triangles), 1D-DBL (up-triangles), 2D-DBL, (circles) and without DBLs (diamonds).

(B) The electronic conductivity of Ag films with 0D-DBL (down-triangles), 1D-DBL (up-triangles), 2D-DBL (circles), and without DBLs (diamonds).

(C and D) The steady-state photoluminescence spectra (C) and the time-resolved photoluminescence spectra (D) of perovskite films with or without DBLs.

estimate the amount of remaining volatile iodide by measuring the characteristic light absorbance of perovskite film.

According to Fick's law, the diffusion equation can be expressed as:

$$\frac{\partial C}{\partial t} = D_0 \cdot \exp\left(-\frac{E_A}{k_B T}\right) \cdot \frac{\partial^2 C}{\partial x^2} = D_T \cdot \frac{\partial^2 C}{\partial x^2} \qquad \text{(Equation 1)}$$

where C is the concentration of mobile iodide remaining in the perovskite films, D_T is the diffusion coefficient at temperature T, E_A is the activation energy of diffusion, k_B is the Boltzmann constant, x is the distance to perovskite surface, and t is the time of diffusion.

As shown in Figure 3A, the perovskite films without DBLs lost most of the characteristic light absorbance after heating aging for 100 h, while only presenting negligible loss when the diffusion of iodide species was blocked by 2D-DBL. We simulated the data by Fick's law and obtained the diffusion coefficients of 4.5×10^{-16} cm^2 s^{-1}, 8.0×10^{-18} cm^2 s^{-1}, and 1.9×10^{-19} cm^2 s^{-1}, for 0D-, 1D-, and 2D-DBL, respectively. These values are 10^3~10^7 times smaller than that in perovskite films (~10^{12} cm^2 s^{-1}),[32] which demonstrate that the diffusion can be well controlled by the DBLs.

The large variation in diffusion coefficients indicates that the capability of controlling iodide diffusion mainly relies on the structure of barrier materials. The 0D-DBL

consists of Al_2O_3 nanoparticles with a size of about 20∼50 nm (Figure S5A). Nanometer-sized pores might still exist in the film, whose size is larger than that of iodide ions (diameter 0.4 nm). Thus, 0D-DBL demonstrated a limited capability in controlling the iodide diffusion process. In 1D-DBL, the polymers were randomly cross-linked to form a film (Figure S5B). The relatively low diffusion coefficient for 1D-DBL may be due to the interchain interactions that can largely reduce the amount of diffusion channels. In case of 2D-DBL, g-C_3N_4 is chemically stable and compact with very few pinholes and channels (∼0.3 nm) that are smaller than the diameter of iodide. In addition, the typical size of g-C_3N_4 is larger than 500 nm (Figures S5C and S6). The possible diffusion channel for iodide species is to bypass g-C_3N_4. The diffusion distance is, therefore, largely increased and the iodide concentration gradient along the diffusion path is reduced accordingly. As a consequence, the total diffusion flux of iodide out from the perovskite film was suppressed effectively. We noted that there were still diffusion channels within 2D-DBL. Larger g-C_3N_4 or other compact two-dimensional materials with robust structures are expected to provide more promising protection from the diffusion-induced degradation of perovskite devices.

Blocking the iodide diffusion by the 2D-DBLs reduces the damage to the Ag interconnects, where well-protected conductivity is essential for high-efficiency PSC modules during the stability test. For unprotected Ag connects, the electronic conductivity decreased very fast, owing to the enhanced corrosion by iodide (Figure 3B). The degradation of the Ag interconnect was scrutinized by X-ray photoelectron spectroscopy (XPS) (Figure S7). It shows that the iodide signal from Ag connect increased more than 10 times after the aging, indicating rapid ingression of iodide from the perovskite film into the Ag electrode. The SEM images show that the morphology of Ag electrode changed from a continuous film to clusters (Figure S8) without DBL, which resulted in the loss in electronic conductivity. With the protection of 0D-and 1-DBLs, though the Ag film degraded slowly, the morphology of Ag electrode has been broken into some clusters. With the protection of 2D-DBLs, the Ag electrode remains unchanged, and only negligible iodide signal was found in the Ag electrode (Figure S6). The conductivity decreased very slowly with the best performance enabled by the 2D-DBL (Figure 3B).

We also studied the effect of DBLs on the photoexcited charge carriers by steady-state and time-resolved photoluminescence (PL) spectroscopy. As shown in Figure 3C, the steady-state PL was increased in case of perovskite/2D-DBL or perovskite/1D-DBL films in comparison with the perovskite film without DBLs. Figure 3D shows the PL decay of the perovskite films with or without DBLs. The PL lifetime for perovskite film with 2D-DBL was 219 ns, longer than that of 164 ns, 124 ns, and 156 ns for perovskite/1D-DBL, perovskite/0D-DBL, and perovskite films, respectively. These results indicate 2D-DBL has a distinct capability to reduce the recombination loss by passivating the surface of perovskite film, which is important for high-efficiency PSC modules. We therefore, expect the 2D-DBL to reduce the charge carrier recombination both at the active area and interconnection area when it implements the major function to reduce the diffusion-induced degradation of PSC modules.

Then, we studied the performance of PSC modules that contain ten sub-cells in series connection (Figure 4B) with the cell structure of NiO/perovskite/N-doped graphene fullerene derivative phenyl-C61-butyric acid methyl ester/BCP/Ag. The cross-section SEM image of the sub-cell is given in Figure 4A and the corresponding energy band structure is shown in Figure 4C. In the PSC modules, a thick 2D-DBL was

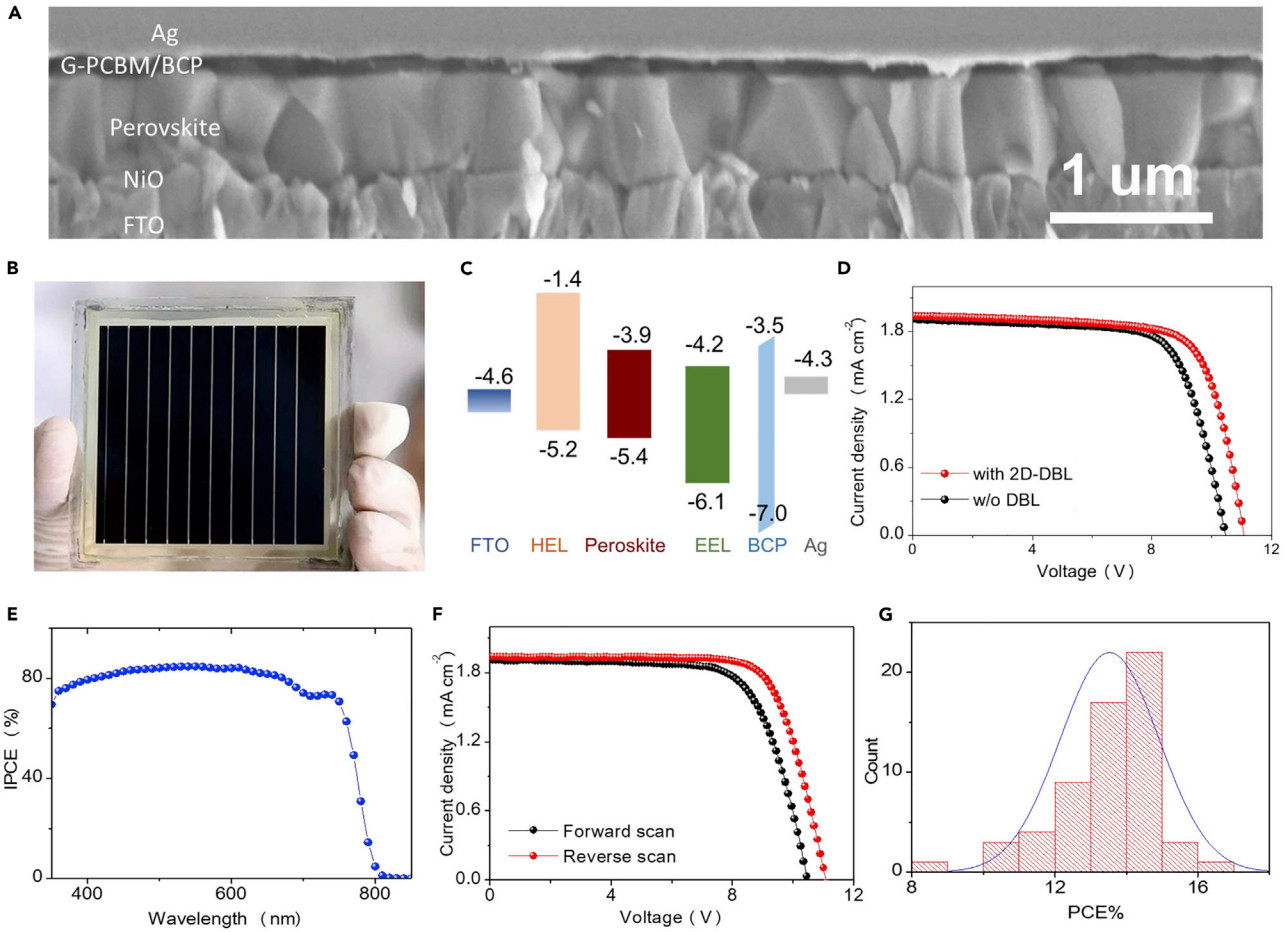

Figure 4. Performance of Perovskite Solar Cell Modules

(A) The cross-section SEM image of the sub-cell.

(B) The photo of the device.

(C) Energy band structure of the sub-cell with a thin g-C_3N_4 layer as 2D-DBL. The HEL here is NiO as the hole extraction layer. The DBL is g-C_3N_4 and the EEL is G-PCBM as the electron extraction layer.

(D) The current-voltage curve of the device with and without 2D-DBL.

(E) The IPCE (incident photon-to current conversion efficiency) spectrum of a solar module with DBL. The integrated current density from IPCE data was 1.95 mA cm^{-2}, which is corresponding to that of the *J-V* results.

(F) *J–V* curves of a solar module with DBL measured in reverse (from V_{OC} to I_{SC}) and forward (from I_{SC} to V_{OC}) scan modes under simulated solar light, AM 1.5G, 100 mW cm^{-2}.

(G) The histograms of PCEs for modules with DBL. The 60 modules were measured under 100 mW cm^{-2}, AM 1.5G illumination under forward bias scan.

inserted between perovskite film edge and Ag electrode to control the lateral diffusion in the interconnection region and suppress the recombination between perovskite edge and Ag electrode (Figure 1A). A thin N-doped graphene fullerene derivative phenyl-C61-butyric acid methyl ester DBL was inserted between perovskite film and Ag electrode to control the vertical diffusion in the active region. The current-voltage (*J–V*) characteristics of PSC modules with an area of 36.1 cm^2 were measured in forward bias scan and the PCE was 15.6% for the device with 2D-DBL, which is higher than that of 14.01% for the one without DBLs (Figure 4D) due to an increase in the open-circuit voltage. The short circuit photocurrent density (Jsc) of the 2D-DBL-based device equals 1.95 mA cm^{-2}, which is almost the same as the integrated Jsc from the incident photon-to-current conversion efficiency (IPCE) spectrum (Figure 4E). As the 2D-DBL constructs an electronic barrier between

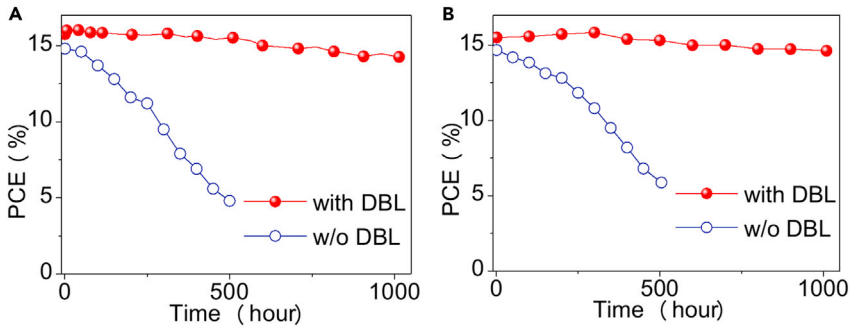

Figure 5. The Performance of Encapsulated Perovskite Modules

(A) In heating aging test at 85°C with relative humidity of about 85% for 1,000 h, and (B) under a UV-filtered simulated sunlight at 60°C in ambient air and maintained at the maximum power point. The power conversion efficiency was measured under simulated AM 1.5 solar light, 100 mW cm^{-2} intensity.

perovskite and Ag, the negligible change in *Jsc* indicates the 2D-DBL can offer efficient interfacial charge transfer between sub-cells. The 2D-DBL-based devices also exhibited a small hysteresis in *J–V* characteristics (Figure 4F) and good reproducibility (Figure 4G).

The PSC modules were encapsulated and stored under 85°C and 85% relative humidity in a chamber and were taken out of the chamber to measure the *J–V* curves at an ambient condition with a maximum-power-tracking program until the efficiency is stabilized. The PSC module without DBLs degraded very fast from 14.7% to 5.9% within 500 h (Figure 5A), which is much poorer than that of small-area PSCs (Figure S9). The degradation comprises a 37% loss in fill factor (*FF*), 44% in short current photocurrent density (*Jsc*), and 8% in open-circuit voltage (*Voc*). For PSC modules with DBL, it obtained a stable PCE with 95% of the initial value after 1,000 h under heating aging test. We show the light stability of PSC modules kept under AM 1.5G simulated solar light (Figure 5B). The PCE of the module with DBL also exhibited good light stability with 91% of the initial value after 1,000 h aging test. It should be noted that the $[CH(NH_2)_2]_{0.85}[CH_3NH_3]_{0.15}Pb(I_{0.85}Br_{0.15})_3$-based PSC module exhibits better stability than $CH_3NH_3PbI_3$-based device (Figures S10 and S11), which confirms that CH_3NH_3I is the major diffusive constituent within perovskite devices. One of our modules covered by a black mask with an aperture area of 6.0 × 6.0 cm was sent to an accredited independent photovoltaic test laboratory (Newport Corporation PV Lab, Montana, USA) for certification. The device with a photomask area of 35.8 cm^2 still displayed a certified PCE of 14.17% ± 0.44% (Figure S12) after heating aging test.

The transient photovoltage (TPV) and transient photocurrent (TPC) are given in Figure S13 for PSC modules aged for 500 h. The charge recombination lifetime of the module treated with 2D-DBLs was obviously larger than that without DBLs, resulting in higher *Voc* of 2D-DBL-based devices. The faster TPC decay in 2D-DBLs-based module is consistent with the efficient interfacial charge transfer between sub-cells, which leads to the generation of high photocurrent density. These results indicate the 2D-DBL played a key role in maintaining the optoelectronic conversion process within PSC modules.

The series resistance (Rs) at interconnection region (Figure S14) increased 3 times in magnitude during the aging test for PSC modules with no DBLs, while it only increased negligibly in the one with 2D-DBL. The interconnection region without

DBLs turned yellow, consistent with the common degradation from perovskite to PbI_2 (Figure S15). The characteristic absorbance of PbI_2 at 520 nm and light absorbance loss of $MAPbI_3$ were identified near the interconnection region (Figure S16). For the PSC modules with 1D- or 2D-DBL, there is no obvious change in color or loss of light absorbance at the interconnection region, indicating that the PSC modules were well protected. As shown in Figure S17, the optical micrograph demonstrates Ag electrode without DBLs at the interconnection region was corroded seriously and the continuous film was broken. The SEM images (Figure S18) show that Ag electrode was smooth before aging test and then became very rough after aging for 360 h. More than 90% Ag of the interconnect disappeared, which hampered the conduction of photocurrent. In contrast, with the protection of 2D-DBLs, the Ag electrode maintained integrity without apparent corrosion in the interconnection region (Figure S19).

This work demonstrates that the extra diffusion-induced degradation of high-efficiency PSC modules was largely suppressed by the introduction of diffusion barriers. Ultraslow defect diffusion was enabled as the unfavorable defect diffusion through nanoscale tunnels was well hindered. In addition, the electronic structures of DBLs have advantages in suppressing the charge recombination and offering rapid interfacial charge transfer. Our findings are of importance for the design and realization of highly stable and efficient perovskite-based solar modules and optoelectronic devices.

EXPERIMENTAL PROCEDURES

Preparation of Ultra-thin *g*-C_3N_4 Nanosheets

The ultra-thin *g*-C_3N_4 nanosheet was fabricated following a "bulk-nanosheet to ultra-thin nanosheet" route. Briefly, the bulk *g*-C_3N_4 was ground into powder in a mortar and transferred to a ceramic boat, followed by annealing at 500°C for 3 h. A light yellow powder of *g*-C_3N_4 nanosheets was obtained. Subsequently, 500 mg of *g*-C_3N_4 ultra-thin nanosheets were dispersed in 500 mL of isopropyl alcohol at room temperature and were exfoliated by ultrasonication for 2 h. The final product was centrifuged and dried at 60°C for 8 h via removing water in a freeze-dryer.

Preparation of Diffusion Barrier Materials

To solidify the DBL coating at low temperature, we make photocurable coating by UV light at room temperature. The functionalized DBL material with a bit of epoxy resin was cured by cationic photopolymerization to enhance mechanical properties and strength of adhesion to various substrates. The formula and preparation methods are as follows: DBL materials and the epoxy resin in the 19:0.8 weight ratio was directly dispersed in chloroform (80 wt % total dry content). To reach a good dispersion of the DBL materials in the epoxy resin, the above solution was treated by means of stirring for 1 h and ultrasonic bath for 10 h. After mixing, 0.2 wt % photo-initiator (triphenylsulfonium hexafluoroantimonate) was added to the above formulation with an ultrasonic bath for 10 h. All above DBL solutions were wrapped by the aluminum foil before use.

Fabrication of Solar Modules

The schematic of fabrication procedure including all scribing and deposition steps are as follows (Figure S20):

Step 1

The fabricating process of the perovskite solar module was similar to that of small solar cells except for the dosage of the precursor and the laser scribing patterning process. Firstly, the FTO-coated glass (NSG) was etched by laser process with a

1,064 nm wavelength. We used a pulse laser with a pulse energy of 30 μJ, a spot size of 25 μm, a pulse frequency of 30 kHz, and a slow scribing speed of 50 mm s^{-1} to scribe FTO substrates with a line width of 100 μm^3. Then the substrates were washed with soap (2% Hellmanex in water), deionized water, acetone, and ethanol and finally treated under oxygen plasma for 10 min to remove the last traces of organic residues.

Step 2

Then, 60 ml of an acetonitrile/ethanol (with 95:5 volume ratio) solution of nickel acetylacetonate (with 5 mol % magnesium acetate tetrahydrate) was sprayed by an air nozzle onto the hot FTO glasses at 570°C. A dense hole transfer layer of NiO (about 20 nm in thickness) was prepared onto the FTO substrate. The perovskite precursor was an amine complex precursor and used the acetonitrile as solvent. Briefly, for the $MAPbI_3$ perovskite precursor, 1 mol/ml CH_3NH_3I and 1 mol/ml PbI_2 powders were mixed in a bottle with acetonitrile. The dried CH_3NH_2 gas was passed into a bottle with a constant flow rate of 0.5 L min^{-1}. The yellow liquid was obtained after CH_3NH_2 gas flushing for 1 min. It was further stirred under an atmosphere of flowing CH_3NH_2 gas at room temperature for about 30 min. For the $[CH(NH_2)_2]_{0.85}[CH_3NH_3]_{0.15}Pb(I_{0.85}Br_{0.15})_3$, the precursor solution of mixed perovskite consists of 424 mg FAI, 1,136 mg PbI_2, 49 mg CH_3NH_3Br, and 160 mg $PbBr_2$ dissolved in 2.4 ml acetonitrile. Then the powers turned to a liquid state after dried CH_3NH_2 passed with the same process above. The perovskite film was prepared by slot-die method. Briefly, the perovskite precursor solution was pumped into the slot-die coating head. The distance between the bottom of slot-die coating head and the top of the glass substrate was set at 0.5 mm. The pumping rate was 100 μl/min and the coater belt speed was 4.2 mm/sec. The coated precursors were annealed at 110°C for 15 min. DBL on perovskite film was on the perovskite film by spin-coating its 2 mg/ml chloroform solution for 30 s with 6,000 r.p.m. The G-PCBM solution (30 mg/ml, PCBM in chlorobenzene with 2 wt % graphene) was dissolved at 50°C by stirring for 12 h before use. The G-PCBM was deposited on the DBL/perovskite/NiO/FTO substrate by spin-coating for 30 s with 1,500 r.p.m. Then 8 nm BCP was thermally evaporated under high vacuum (lower than $2X10^{-5}$ Pa).

Step 3

After that, the laser scribing process was conducted with 532 nm wavelength. The laser pulse energy was 10 μJ with a spot size of 25 μm and the pulse frequency of 20 kHz and the scribing speed of 100 mm s^{-1} to scribe a line width of 300 μm.

Step 4

After the laser process, the DBL material solution was injected into the interconnection region. Specially, the DBL solution was injected into the interconnection region after it was added into the injection syringe of automatic glue dispenser robot (Worldwide Technology) with an X/Y/Z-axis working range of 400 × 400 × 150 mm. The DBL materials solution was injected into the interconnection of modules by controlling the injection rate and the movement speed of syringe fixed on the glue dispenser robot. The space between the bottom of the syringe needle and the surface of below module is 0.8 mm. The DBL solution was glued into the interconnection region line of modules with an injection rate of 30 ul/min and the movement speed of 20 mm/s. Finally, the diffusion barrier materials were cured to the solid-state for 60 s by the UV irradiation with the irradiation intensity of 25 mW cm^{-2}. Then the laser scribing process was conducted to scribing the excrescent DBL. The laser pulse energy was 12 μJ with a spot size of 25 μm and the pulse

frequency of 30 kHz and the scribing speed of 60 mm s^{-1} to scribe a line width of 200 μm.

Step 5

The 100 nm of Ag was thermally evaporated under high vacuum (lower than 2×10^{-5} Pa).

Step 6

Then the laser separated the Ag electrode, this was carried out with a pulse energy of 20 μJ, with a spot size of 25 μm, a pulse frequency of 60 kHz, and a scribing speed of 80 mm s^{-1} to scribe the Ag electrode with a line width of 80 μm. Finally, the solar module was sealed by UV glue coating on a cavity glass which covered the space between the front FTO glass and the active films.

Characterization and Measurement

The morphologies of as-obtained products were measured using a field-emission scanning electron microscope (SEM, JEOLJSM-7800F). Ultraviolet-visible absorption spectra were recorded on a Shimadzu UV 2550 spectrophotometer in the 200–1,000 nm wavelength range at room temperature. The crystal structures of perovskite film were characterized by powder X-ray diffraction (XRD) using a Goniometer Ultima IV (185nm) diffractometer with Cu Kα radiation, excited at 40 kV and 40 mA.

The current-density (*J*)-voltage (*V*) curves (*J–V* curves) measurement employed a black metal mask with an aperture area of 36.1 cm^2. The J-V curves of the perovskite solar cells were measured with a digital source meter (Keithley 2400) under simulated solar illumination at 100 mW cm^{-2}, AM 1.5G standard air mass sunlight (Newport, Oriel Class A, 91195A). The simulated light intensity was calibrated by a Si-reference cell certified by the Calibration, Standards, and Measurement Team at the Research Center for Photovoltaics in AIST, Japan. The spectral mismatch is less than 3%. The J–V curves were measured by forward (from −2 to 12 V) scan. The step voltage was fixed at 50 mV and the delay time was 50 ms. The light-soaking stability was tested in a solar cell light resistance test system (Model BIR-50, Bunkoh-Keiki Co., LTD) equipped with a Class AAA solar simulator; <420 nm UV light was cut off with an optical filter. Monochromatic incident photon-to-current conversion efficiency (IPCE) spectra were measured with a monochromatic incident light of 1×10^{16} photons cm^{-2} in director current mode.

Transient photovoltage and photocurrent decay curves were measured on a home-made system with a white light bias generated from an array of diodes (100 mW cm^{-2}), and a red light pulse diode (0.05 s square pulse width, 100 ns rise and fall time, 5 mW cm^{-2}) controlled by a fast solid-state switch was used as the perturbation source. The transient photocurrent was measured using 20 Ohm external series resistance to operate the device in the short circuit. Similarly, transient photovoltage was measured using 1 MΩ external series resistance to operate the device in the open circuit. The voltage dynamics on the resistors were recorded on a digital oscilloscope (Tektronix MDO3032). The perturbation of the red light source was set to a suitably low level than the white diodes array with a light intensity equivalent to 100 mW cm^{-2} of a standard solar simulator.

SUPPLEMENTAL INFORMATION

Supplemental Information can be found online at https://doi.org/10.1016/j.joule.2019.07.030.

ACKNOWLEDGMENTS

This work was supported by National Key Research and Development Program of China (grant no. 2018YFB1500104), the National Natural Science Foundation of China (grant no. 11574199, 11674219, and 11834011), the Program for Professor of Special Appointment (Eastern Scholar) at Shanghai Institutions of Higher Learning, the Program for National Postdoctoral Program for Innovative Talents and the National Postdoctoral Foundation of China (2018M640388), and the Natural Science Foundation of Shanghai (17ZR1414800). X.Y. thanks Dr. Yuanjian Zhang from Southeast University for helpful discussion. The authors thank the Instrumental Analysis Center of SJTU and Advanced Electronic Materials and Devices (AEMD) of SJTU for measurements.

AUTHOR CONTRIBUTIONS

L.H. and X.Y. designed and directed the study. E.B., W.T., and C.H. conceived and performed the main experimental work. Y.W., T.W., W.K., J.H., and S.K. contributed to the characterization. J.B. and X.Z. conducted the simulation of defect diffusion. X.Y. and E.B. analyzed the data. X.Y, M.G, and L.H. wrote the manuscript. All authors reviewed the paper.

DECLARATION OF INTERESTS

The authors declare no competing interests.

Received: May 15, 2019
Revised: July 4, 2019
Accepted: July 29, 2019
Published: September 3, 2019

REFERENCES

1. Kojima, A., Teshima, K., Shirai, Y., and Miyasaka, T. (2009). Organometal halide perovskites as visible-light sensitizers for photovoltaic cells. J. Am. Chem. Soc. *131*, 6050–6051.

2. Im, J.H., Lee, C.R., Lee, J.W., Park, S.W., and Park, N.G. (2011). 6.5% efficient perovskite quantum-dot-sensitized solar cell. Nanoscale *3*, 4088–4093.

3. Kim, H.S., Lee, C.R., Im, J.H., Lee, K.B., Moehl, T., Marchioro, A., Moon, S.J., Humphry-Baker, R., Yum, J.H., Moser, J.E., et al. (2012). Lead iodide perovskite sensitized all-solid-state submicron thin film mesoscopic solar cell with efficiency exceeding 9%. Sci. Rep. *2*, 591.

4. Lee, M.M., Teuscher, J., Miyasaka, T., Murakami, T.N., and Snaith, H.J. (2012). Efficient hybrid solar cells based on meso-superstructured organometal halide perovskites. Science *338*, 643–647.

5. Mailoa, J.P., Bailie, C.D., Johlin, E.C., Hoke, E.T., Akey, A.J., Nguyen, W.H., McGehee, M.D., and Buonassisi, T. (2015). A 2-terminal perovskite/silicon multijunction solar cell enabled by a silicon tunnel junction. Appl. Phys. Lett. *106*.

6. Burschka, J., Pellet, N., Moon, S.J., Humphry-Baker, R., Gao, P., Nazeeruddin, M.K., and Grätzel, M. (2013). Sequential deposition as a route to high-performance perovskite-sensitized solar cells. Nature *499*, 316–319.

7. Liu, M., Johnston, M.B., and Snaith, H.J. (2013). Efficient planar heterojunction perovskite solar cells by vapour deposition. Nature *501*, 395–398.

8. Chen, Q., Zhou, H., Hong, Z., Luo, S., Duan, H.S., Wang, H.H., Liu, Y., Li, G., and Yang, Y. (2014). Planar heterojunction perovskite solar cells via vapor-assisted solution process. J. Am. Chem. Soc. *136*, 622–625.

9. Zhou, H., Chen, Q., Li, G., Luo, S., Song, T.B., Duan, H.S., Hong, Z., You, J., Liu, Y., and Yang, Y. (2014). Photovoltaics. Interface engineering of highly efficient perovskite solar cells. Science *345*, 542–546.

10. Chen, W., Wu, Y., Yue, Y., Liu, J., Zhang, W., Yang, X., Chen, H., Bi, E., Ashraful, I., Grätzel, M., et al. (2015). Efficient and stable large-area perovskite solar cells with inorganic charge extraction layers. Science *350*, 944–948.

11. Yang, W.S., Noh, J.H., Jeon, N.J., Kim, Y.C., Ryu, S., Seo, J., and Seok, S.I. (2015). High-performance photovoltaic perovskite layers fabricated through intramolecular exchange. Science *348*, 1234–1237.

12. Jiang, Q., Chu, Z., Wang, P., Yang, X., Liu, H., Wang, Y., Yin, Z., Wu, J., Zhang, X., and You, J. (2017). Planar-structure perovskite solar cells with efficiency beyond 21%. Adv. Mater. *29*.

13. Zheng, X., Chen, B., Dai, J., Fang, Y., Bai, Y., Lin, Y., Wei, H., Zeng, X.C., and Huang, J. (2017). Defect passivation in hybrid perovskite solar cells using quaternary ammonium halide anions and cations. Nat. Energy *2*, 17102.

14. Li, C., Zhou, Y., Wang, L., Chang, Y., Zong, Y., Etgar, L., Cui, G., Padture, N.P., and Pang, S. (2017). Methylammonium-mediated evolution of mixed-organic-cation perovskite thin films: a dynamic composition-tuning process. Angew. Chem. Int. Ed. *56*, 7674–7678.

15. Cai, M., Wu, Y., Chen, H., Yang, X., Qiang, Y., and Han, L. (2017). Cost-performance analysis of perovskite solar modules. Adv. Sci. *4*, 1600269.

16. Green, M.A. (2016). Commercial progress and challenges for photovoltaics. Nat. Energy *1*, 15015.

17. Grancini, G., Roldán-Carmona, C., Zimmermann, I., Mosconi, E., Lee, X., Martineau, D., Narbey, S., Oswald, F., De Angelis, F., Graetzel, M., et al. (2017). One-year stable perovskite solar cells by 2D/3D interface engineering. Nat. Commun. *8*, 15684.

18. Hu, Y., Si, S., Mei, A., Rong, Y., Liu, H., Li, X., and Han, H. (2017). Stable large-area (10× 10 cm2) printable mesoscopic perovskite module exceeding 10% efficiency. Sol. RRL *1*.

19. Mei, A., Li, X., Liu, L., Ku, Z., Liu, T., Rong, Y., Xu, M., Hu, M., Chen, J., Yang, Y., et al. (2014). A hole-conductor-free, fully printable

mesoscopic perovskite solar cell with high stability. Science *345*, 295–298.

20. Jeon, N.J., Noh, J.H., Yang, W.S., Kim, Y.C., Ryu, S., Seo, J., and Seok, S.I. (2015). Compositional engineering of perovskite materials for high-performance solar cells. Nature *517*, 476–480.

21. Saliba, M., Matsui, T., Domanski, K., Seo, J.Y., Ummadisingu, A., Zakeeruddin, S.M., Correa-Baena, J.P., Tress, W.R., Abate, A., Hagfeldt, A., et al. (2016). Incorporation of rubidium cations into perovskite solar cells improves photovoltaic performance. Science *354*, 206–209.

22. McMeekin, D.P., Sadoughi, G., Rehman, W., Eperon, G.E., Saliba, M., Hörantner, M.T., Haghighirad, A., Sakai, N., Korte, L., Rech, B., et al. (2016). A mixed-cation lead mixed-halide perovskite absorber for tandem solar cells. Science *351*, 151–155.

23. Tan, H., Jain, A., Voznyy, O., Lan, X., García de Arquer, F.P.G., Fan, J.Z., Quintero-Bermudez, R., Yuan, M., Zhang, B., Zhao, Y., et al. (2017). Efficient and stable solution-processed planar perovskite solar cells via contact passivation. Science *355*, 722–726.

24. Hou, Y., Du, X., Scheiner, S., McMeekin, D.P., Wang, Z., Li, N., Killian, M.S., Chen, H., Richter, M., Levchuk, I., et al. (2017). A generic interface to reduce the efficiency-stability-cost gap of perovskite solar cells. Science *358*, 1192–1197.

25. Luo, D., Yang, W., Wang, Z., Sadhanala, A., Hu, Q., Su, R., Shivanna, R., Trindade, G.F., Watts, J.F., Xu, Z., et al. (2018). Enhanced photovoltage for inverted planar heterojunction perovskite solar cells. Science *360*, 1442–1446.

26. Tsai, H., Nie, W., Blancon, J.C., Stoumpos, C.C., Asadpour, R., Harutyunyan, B., Neukirch, A.J., Verduzco, R., Crochet, J.J., Tretiak, S., et al. (2016). High-efficiency two-dimensional Ruddlesden–Popper perovskite solar cells. Nature *536*, 312–316.

27. Swarnkar, A., Marshall, A.R., Sanehira, E.M., Chernomordik, B.D., Moore, D.T., Christians, J.A., Chakrabarti, T., and Luther, J.M. (2016). Quantum dot-induced phase stabilization of α-CsPbI3 perovskite for high-efficiency photovoltaics. Science *354*, 92–95.

28. Bella, F., Griffini, G., Correa-Baena, J.P., Saracco, G., Grätzel, M., Hagfeldt, A., Turri, S., and Gerbaldi, C. (2016). Improving efficiency and stability of perovskite solar cells with photocurable fluoropolymers. Science *354*, 203–206.

29. Arora, N., Dar, M.I., Hinderhofer, A., Pellet, N., Schreiber, F., Zakeeruddin, S.M., and Grätzel, M. (2017). Perovskite solar cells with CuSCN hole extraction layers yield stabilized efficiencies greater than 20%. Science *358*, 768–771.

30. Mizusaki, J., Arai, K., and Fueki, K. (1983). Ionic conduction of the perovskite-type halides. Solid State Ion. *11*, 203–211.

31. Zhou, W., Zhao, Y., Zhou, X., Fu, R., Li, Q., Zhao, Y., Liu, K., Yu, D., and Zhao, Q. (2017). Light-independent ionic transport in inorganic perovskite and ultrastable Cs-based perovskite solar cells. J. Phys. Chem. Lett. *8*, 4122–4128.

32. Eames, C., Frost, J.M., Barnes, P.R., O'regan, B.C., Walsh, A., and Islam, M.S. (2015). Ionic transport in hybrid lead iodide perovskite solar cells. Nat. Commun. *6*, 7497.

33. Kato, Y., Ono, L.K., Lee, M.V., Wang, S., Raga, S.R., and Qi, Y. (2015). Silver iodide formation in methyl ammonium lead iodide perovskite solar cells with silver top electrodes. Adv. Mater. Interfaces *2*.

34. Jiang, Y., Remeika, M., Hu, Z., Juarez-Perez, E.J., Qiu, L., Liu, Z., Kim, T., Ono, L.K., Son, D.Y., Hawash, Z., et al. (2019). Negligible-Pb-waste and upscalable perovskite deposition technology for high-operational-stability perovskite solar modules. Adv. Energy Mater. *9*.

35. Yuan, Y., Chae, J., Shao, Y., Wang, Q., Xiao, Z., Centrone, A., and Huang, J. (2015). Photovoltaic switching mechanism in lateral structure hybrid perovskite solar cells. Adv. Energy Mater. *5*.

36. Chen, H., Ye, F., Tang, W., He, J., Yin, M., Wang, Y., Xie, F., Bi, E., Yang, X., Grätzel, M., et al. (2017). A solvent-and vacuum-free route to large-area perovskite films for efficient solar modules. Nature *550*, 92–95.

37. Bi, E., Chen, H., Xie, F., Wu, Y., Chen, W., Su, Y., Islam, A., Grätzel, M., Yang, X., and Han, L. (2017). Diffusion engineering of ions and charge carriers for stable efficient perovskite solar cells. Nat. Commun. *8*, 15330.

38. Li, Z., Klein, T.R., Kim, D.H., Yang, M., Berry, J.J., van Hest, M.F.A.M., and Zhu, K. (2018). Scalable fabrication of perovskite solar cells. Nat. Rev. Mater. *3*, 18017.

39. Boyd, C.C., Cheacharoen, R., Bush, K.A., Prasanna, R., Leijtens, T., and McGehee, M.D. (2018). Barrier design to prevent metal-induced degradation and improve thermal stability in perovskite solar cells. ACS Energy Lett. *3*, 1772–1778.

40. Dualeh, A., Gao, P., Seok, S.I., Nazeeruddin, M.K., and Grätzel, M. (2014). Thermal behavior of methylammonium lead-trihalide perovskite photovoltaic light harvesters. Chem. Mater. *26*, 6160–6164.